

# Coherent single-spin control with high-fidelity singlet-triplet readout in silicon

R. Zhao,<sup>1,\*</sup> T. Tantt,<sup>1</sup> K. Y. Tan,<sup>2</sup> B. Hensen,<sup>1</sup> K. W. Chan,<sup>1,†</sup> J. C. C. Hwang,<sup>1,‡</sup> R. C. C. Leon,<sup>1</sup> C. H. Yang,<sup>1</sup> W. Gilbert,<sup>1</sup> F. E. Hudson,<sup>1</sup> K. M. Itoh,<sup>3</sup> A. A. Kiselev,<sup>4</sup> T. D. Ladd,<sup>4</sup> A. Morello,<sup>1</sup> A. Laucht,<sup>1</sup> and A. S. Dzurak<sup>1</sup>

<sup>1</sup>Centre for Quantum Computation & Communication Technology,  
School of Electrical Engineering & Telecommunications,

University of New South Wales, Sydney, New South Wales 2052, Australia

<sup>2</sup>QCD Labs, COMP Centre of Excellence, Department of Applied Physics, Aalto University, 00076 AALTO, Finland

<sup>3</sup>School of Fundamental Science and Technology, Keio University,  
3-14-1 Hiyoshi, Kohoku-ku, Yokohama 223-8522, Japan

<sup>4</sup>HRL Laboratories, LLC, 3011 Malibu Canyon Rd., Malibu, CA 90265, USA

(Dated: December 15, 2024)

Single electron spins in silicon can be used to realize quantum bits (qubits) that profit from the long coherence times inherent to the host material<sup>1-4</sup>. When confined in quantum dots (QDs) using electrostatic gates, there is the added promise of scalability by leveraging industrial semiconductor manufacturing technology<sup>5-8</sup>. However, most single-electron spin qubits produced to date employ quantum state readout via spin-dependent-tunnelling to an electron reservoir<sup>9</sup>. This requires significant on-chip real estate, limiting the prospects for large scale multi-qubit systems. Here, we address this challenge by combining coherent single-spin control with high-fidelity, single-shot, singlet-triplet readout. We employ Pauli spin blockade in a double QDs as a readout tool to achieve a measurement fidelity of 99.3 %. This allows us to implement coherent electron spin resonance (ESR) control at magnetic fields as low as 150 mT, corresponding to a carrier frequency of 4.2 GHz, eliminating the need for high-frequency microwave sources. We discover that the qubits decohere faster at low magnetic fields with  $T_2^{\text{Rabi}} = 18.6 \mu\text{s}$  and  $T_2^* = 1.4 \mu\text{s}$  at 150 mT. Their coherence is limited by spin flips of residual <sup>29</sup>Si nuclei in the isotopically enriched <sup>28</sup>Si host material, that occur more frequently at lower fields. Our finding highlights the importance of further isotopic enrichment of device substrates for the realization of a scalable silicon-based quantum processor.

The rapid progress of spin qubits in silicon QDs has been fuelled by coherent electron spin resonance (ESR), either driven by an ac magnetic<sup>3</sup> or electric-field<sup>10,11</sup>. To date, ESR has enabled the demonstration of high-fidelity single- and two-qubit logic gates approaching the fault tolerance threshold<sup>12-17</sup>. In most of these demonstrations, single-shot spin readout was performed via spin-selective tunnelling of a single spin to a reservoir<sup>9</sup>, however this technique is problematic for the operation of large-scale multi-qubit architectures<sup>6,18</sup>. In order to work, it would require complex, coherent single-spin shuttling<sup>19,20</sup> or a chain of swap gate opera-

tions<sup>21</sup> to readout qubits distant from a reservoir. Furthermore, quantum error correction protocols require simultaneous spin-state readout at arbitrary locations in the large-scale qubit array<sup>18</sup>. The preferred method for spin-readout is, therefore, singlet-triplet (ST) readout via Pauli spin blockade (PSB) in a double QDs system<sup>22</sup>. Besides alleviating the design constraints imposed by reservoir readout, single-shot dispersive ST readout can also leverage state-of-the-art reflectometry technology to enable gate-based sensors with extremely small on-chip footprint<sup>23-25</sup>. Furthermore, ST readout forms the foundation of parity measurements, a main ingredient of many quantum error correction protocols<sup>18</sup>, and does not require the Zeeman splitting energy to be much larger than the thermal energy, which is a limiting constraint with reservoir-based readout<sup>9</sup>. It therefore constitutes a robust readout technique that allows qubit operation over a wide range of magnetic fields. Low magnetic fields, in particular, are highly desirable because they enable qubit operation at lower spin resonance frequencies, simplifying microwave engineering and requiring less expensive signal generators. Coherent ESR and high-fidelity ST readout are therefore the key elements for the implementation of a scalable, silicon-based quantum processor<sup>6,18</sup>. Previous experiments have shown the compatibility of these two techniques for electrons in GaAs<sup>26,27</sup>, however in silicon, demonstrations using electron spins have so far remained incoherent<sup>21</sup>, while those employing hole spins are yet to achieve single-shot readout<sup>28</sup>.

In this work, we achieve coherent, single-electron spin control with high-fidelity ST readout at a dc magnetic field of 150 mT. The device consists of a linear array of silicon metal-oxide-semiconductor (Si-MOS) QDs, electrostatically defined by a palladium (Pd) gate stack<sup>29</sup> on an isotopically enriched <sup>28</sup>Si epi-layer<sup>30</sup> (see Methods section). Fig. 1a shows a false-coloured scanning electron micrograph of a device nominally identical to the one used in this study. A cross-sectional schematic is plotted in Fig. 1b. We have labelled the QD accumulation gates (G1-G6), the confinement gate (CB) that confines the QDs laterally, the reservoir gate (RG) that accumulates the electron reservoir for loading and unloading electrons, the single-electron transistor (SET)

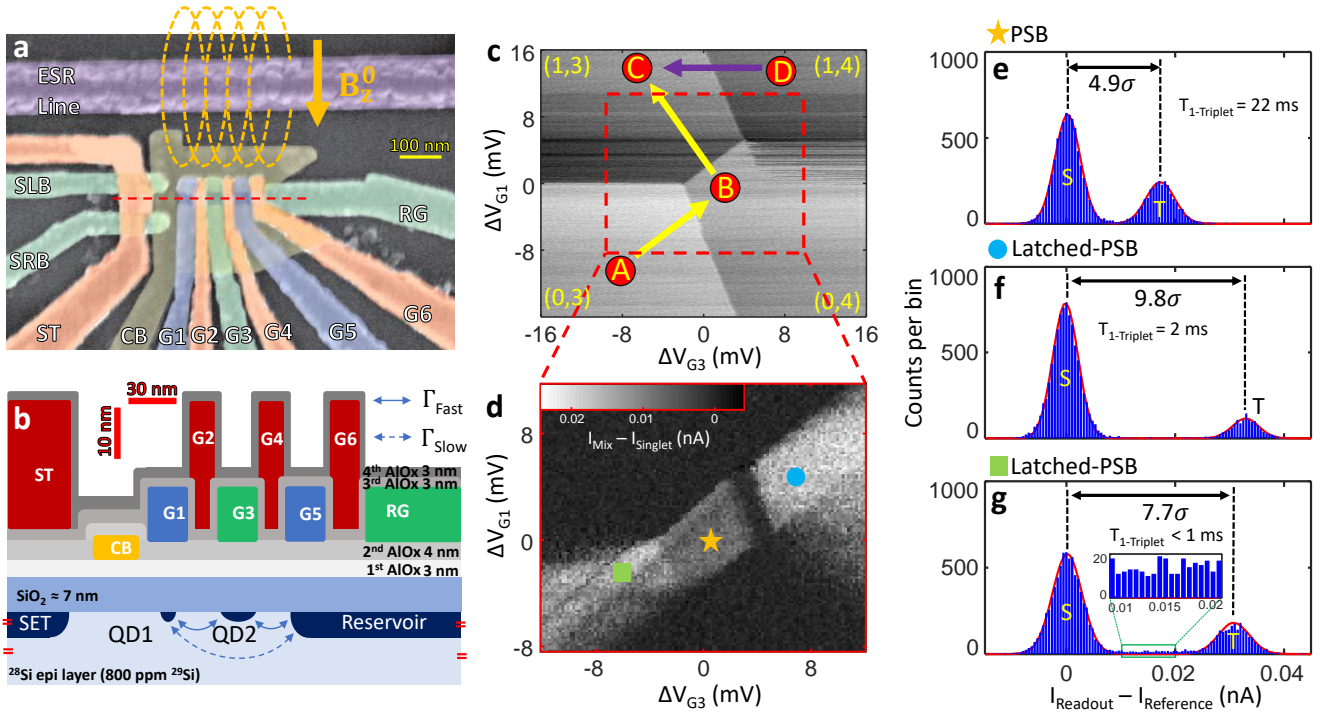


**Figure 1 | Device layout and high-fidelity singlet-triplet readout.** **a**, False-coloured scanning electron micrograph of an identical device. The orange arrow indicates the direction of the dc magnetic field  $B_z^0$ , which is aligned in plane to minimize spin-orbit coupling and reduce the qubits' sensitivity to charge noise. **b**, Cross-sectional schematic along the red dashed line in **a**, showing the Pd gate stack with insulating atomic-layer-deposited aluminium oxide layers. **c**, Charge stability map around the (1,3) - (0,4) anti-crossing. The pulse sequence A-B-C (yellow arrows) prepares a separated double dot with electrons in the singlet state, while the pulse sequence D-C (blue arrow) prepares the double dot in a mixed state. The pulse sequence C-B facilitates the spin readout operation by attempting to push the electron from QD1 into QD2. Tunnelling will occur if the electron in QD1 forms a singlet with the electron in QD2, but it is blocked if the electrons form a triplet. **d**, Difference in SET current between singlet and mixed spin state preparation, plotted as a function of the two gate voltages  $\Delta V_{G1}$  and  $\Delta V_{G3}$ . Apparent are the regions of standard PSB (star) and enhanced latching readout (circle, square). **e-g**, Histograms of the SET current signal for 10200 single-shot readouts with 120  $\mu$ s integration time and 5 pA bin width, using the **e**, standard PSB, or **f,g**, enhanced latching readout regions as indicated by the coloured markers in **d**.

charge sensor (ST, SLB, SRB), and the short of the broadband ESR antenna to apply MW pulses<sup>31</sup> for spin control.

When tuning up the device, we use the following procedure to find the PSB region that gives us high-fidelity, single-shot ST readout. First, we carefully tune all the gate voltages to accumulate two QDs at the approximate locations indicated in Fig. 1b, using the charge sensing technique described in Ref. 32. We then choose the (1,3) - (0,4) anti-crossing, shown in Fig. 1c, as our working point. We assume the first two electrons in QD2 to form a singlet and not to interact with the third and fourth electrons during the experiment. Second, we either initialize the two QDs in a singlet state or in a mixed state of singlet and triplet. When pulsing from point A to point B (yellow arrow) we load a fourth electron on QD2, with the last two electrons forming an anti-parallel spin pair (singlet). Further pulsing to point C will separate these two electrons across the two QDs,

keeping them in the singlet state. Alternatively, when pulsing from point D to C, we will randomly remove one of the four electrons from QD2. The spin of the remaining, third electron could be either anti-parallel or parallel with the spin in QD1, leaving the two QDs initialized in a mix of triplet and singlet. Third, we find the region of PSB, by alternately initializing a singlet and a mixed state, and pulsing to a point around the (1,3) - (0,4) anti-crossing. Fig. 1d plots the difference in the SET current for the two different initializations, performed interleaved to reject slow drifts of the charge sensor. When the two QDs are in the singlet state, the single electron in QD1 can tunnel onto QD2 causing a change in charge configuration from (1,3) to (0,4). However, when they are in the triplet state, tunnelling is inhibited by PSB and the system remains in the (1,3) charge configuration<sup>22</sup>. Therefore, initialization into the mixed state will result in some probability for the charge sensor giving a reading that represents a triplet. We detect

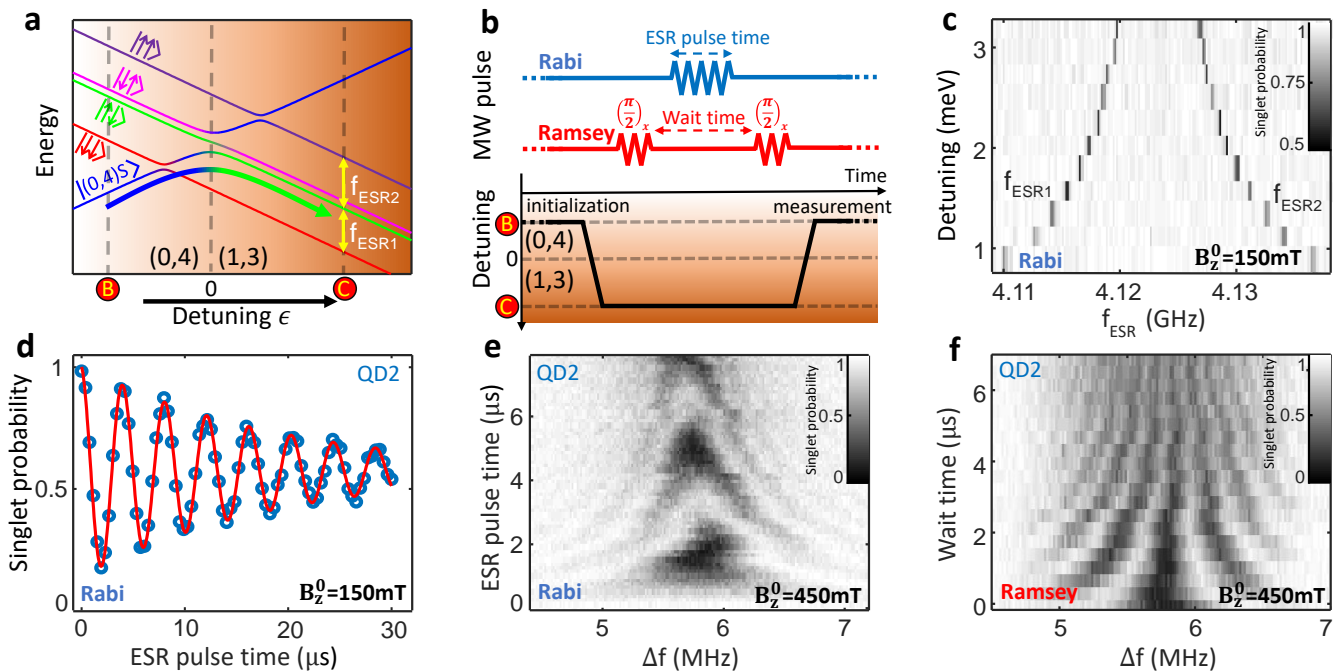


**Figure 2 | Coherent single-spin control with ST readout.** **a**, Schematic energy level diagram of the (1,3) - (0,4) anticrossing. **b**, Partial pulse sequences for the coherent spin control experiments in **d-f**. The sequences start with initializing the system in the (0,4)S state by pulsing from point A to point B (see Fig. 1c). Then we prepare a  $|\uparrow\downarrow\rangle$  by moving from point B to point C. As indicated by the curved colour-graded arrow, we pulse diabatically across the S- $T^-$  anti-crossing, but adiabatically with respect to all the other anti-crossings. We then apply the microwave control pulses at the deep detuning point C to manipulate the individual spins. After spin manipulation, we perform readout by converting  $|\uparrow\downarrow\rangle$  and  $|\downarrow\uparrow\rangle$  into triplet, by pulsing from point C back to the standard PSB region B. The  $|\downarrow\uparrow\rangle$  state is not accessed during this measurement. **c**, The two ESR peaks plotted as a function of detuning  $\epsilon$ . We use an incoherent ESR pulse of 100  $\mu\text{s}$  for this experiment. We identify the lower (higher) frequency peak corresponding to the QD1 (QD2) through the Stark-shift measurements described in Ref. 3. **d-f**, Coherent spin control of QD2 showing **d**, Rabi oscillations, **e**, Rabi chevron, and **f**, Ramsey fringes. We use frequency mixing to implement the ESR pulse scheme.  $\Delta f$  is the difference between the output and the carrier frequencies of the microwave source.

a clear standard PSB region and two enhanced latching regions, in which the very different tunnelling times from the two QDs to the reservoir are used to cause a state dependent change in total charge<sup>33</sup>.

We have designed the orientation of the SET to maximize its sensitivity to inter-dot charge tunnelling events, and achieve good signal contrast for ST readout. As shown in the SET current histogram in Fig. 1e, the signal peaks for standard PSB are separated by  $4.9\sigma$ , indicating a charge state readout fidelity  $> 99.8\%$ . The enhanced latching readout mechanism further increases the signal contrast between the singlet and triplet state, up to  $9.8\sigma$  (see Fig. 1f,g). Such good contrast would allow charge readout with  $< 0.005\%$  error, however we find the latched meta state lifetime to be 2 ms or shorter. This is only one order of magnitude slower than the 120  $\mu\text{s}$  integration time that is required to achieve good signal separation for our experimental setup. Consequently, we notice a non-zero background between the singlet and triplet peaks in Fig. 1g, evidencing decay from the triplet state to the singlet state during measurement. To avoid the spin readout error caused by

the latched meta state relaxation as well as mapping errors<sup>33</sup>, we chose the standard PSB region for readout. The triplet lifetime for standard PSB is 22 ms, which results in a  $\sim 0.5\%$  spin to charge conversion error. This reduces the total fidelity of the single-shot ST readout using standard PSB to 99.3%. The latched metastate lifetime could be improved in future experiments by defining a third electron under G5 to fine-tune the electron tunnelling rate from QD1 and QD2 to the reservoir<sup>35</sup>.

In this study, we control the spins of the electrons using an ac magnetic field generated by the on-chip microwave antenna<sup>31</sup>. In Fig. 2a we plot a schematic of the energy level diagram as a function of energy detuning  $\epsilon$  and in Fig. 2b the pulse sequences that we used to achieve ESR. As shown in Fig. 2c for  $B_z^0 = 150\text{ mT}$ , we find two resonance peaks that correspond to rotations of QD1 (lower frequency) and QD2 (higher frequency). When we decrease  $\epsilon$ , the splitting between the two peaks increases, denoting the larger exchange coupling  $J$  between the electrons and mapping out the energy structure of the (1,3) - (0,4) anticrossing in the shallow

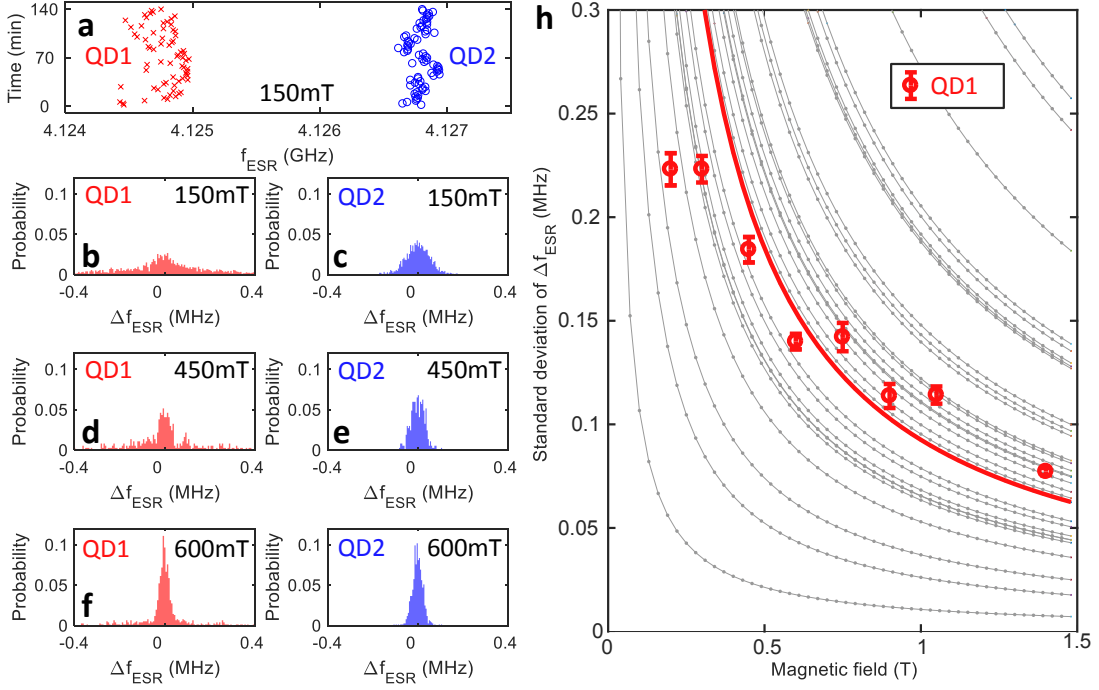


**Figure 3** |  $^{29}\text{Si}$ -induced ESR frequency fluctuations. **a**, Measurement of ESR frequencies of the two qubits over a time period of 140 mins at 150 mT. There are significant fluctuations of the ESR frequencies of both qubits. Each point of measurement lasts about 2 mins. **b-g**, Histograms of ESR frequency fluctuations for both qubits at various magnetic fields. The distribution becomes more concentrated at higher magnetic field. **h**, Red circles show the standard deviation of the fluctuation in ESR frequency of qubit QD1 plotted as a function of magnetic field, with error bars derived as in Ref. 34. Each point is calculated based on a measurement that lasts 8 hours. The red line is a fit  $\propto 1/B_z^0$ . Small gray points, each with gray lines  $\propto 1/B_z^0$ , indicate simulations of  $^{29}\text{Si}$  nuclear spin-flip processes for 30 simulated samples with random nuclear placements. The error bars correspond to the standard error of the sample standard deviation estimated from the raw ESR jump data without any assumptions of the shape of the underlying distribution.

detuning region. Next, we investigate the coherence of the spin qubits in low magnetic fields. By varying the ESR pulse time, we observe clear Rabi oscillations (Fig. 2d) at a magnetic field as low as  $B_z^0 = 150$  mT, with  $T_2^{\text{Rabi}} = 18.6$   $\mu\text{s}$ . In Fig. 2e, we plot the Rabi chevron for one of the qubits at  $B_z^0 = 450$  mT. We also use a Ramsey sequence (Fig. 2f) to measure  $T_2^*$  at various magnetic fields. The observed  $T_2^*$  values are reported in Table I.

The ability to perform coherent control on the spin states allows us to experimentally validate the combined initialization, control and measurement fidelity. We extract the maximum readout visibility for the  $|\uparrow\uparrow\rangle$  state by fitting the Rabi oscillations in Fig. 2d. The maximum visibility is  $87.1 \pm 1.9$  %, which is noticeably lower

$B_z^0$ (mT)	150	300	450
$f_{\text{Rabi}}$ (MHz)	0.25	0.25	0.33
$T_2^*$ ( $\mu\text{s}$ )	$1.4 \pm 0.21$	$2.5 \pm 0.3$	$3.3 \pm 0.65$

TABLE I | Observed  $T_2^*$  at three different magnetic fields  $B_z^0$  with its associated Rabi frequencies  $f_{\text{Rabi}}$ .

than our earlier estimate of the readout fidelity. During this measurement campaign, we observed frequent jumps in the ESR frequencies of both qubits due to spin flip of the surrounding  $^{29}\text{Si}$  nuclei. This renders it difficult to keep the microwave frequency exactly on-resonance for the duration of the measurement (see also Fig. 2e). Therefore, the true readout visibility of the  $|\uparrow\uparrow\rangle$  state may not be reflected in this measurement. We also studied the maximum readout visibility for the three other spin states ( $|\downarrow\uparrow\rangle$ ,  $|\uparrow\downarrow\rangle$  and  $|\downarrow\downarrow\rangle$ ) using complementary measurements. The visibility for  $|\uparrow\downarrow\rangle$  is as high as  $99.5 \pm 0.7$  %, consistent with the readout fidelity estimated previously. The results are summarized in Table II with more details given in the Extended Data Fig. 1 and Supplementary Information.

The robustness of ST readout allows us to employ tracking of the ESR frequency as a tool to study the nuclear spin environment of the spin qubits over a wide range of magnetic fields from  $B_z^0 = 150$  mT to 1.4 T. As already noticeable in Fig. 2e, we observe fluctuations of the ESR frequencies  $\Delta f_{\text{ESR}} = f_{\text{ESR}}(t_2) - f_{\text{ESR}}(t_1)$  of both qubits in time. More detailed data is shown in Fig. 3a, where we track the ESR frequencies of both qubits over 140 mins. There is no correlation between

Spin state	Readout outcome	Visibility	Method	Limitation
$ \uparrow\uparrow\rangle$	Triplet	$87\pm 1.9\%$	ESR driven $ \uparrow\uparrow\rangle \Leftrightarrow  \uparrow\downarrow\rangle$ oscillation	Control
$ \downarrow\uparrow\rangle$	Triplet	$99.3\pm 2.3\%$	Exchange driven $ \downarrow\uparrow\rangle \Leftrightarrow  \uparrow\downarrow\rangle$ oscillation	Readout
$ \uparrow\downarrow\rangle$	Singlet	$99.5\pm 0.7\%$	$ \uparrow\downarrow\rangle \Rightarrow  \downarrow\downarrow\rangle$ $T_1$ relaxation	Readout
$ \downarrow\downarrow\rangle$	Triplet	$96.8\pm 1.0\%$	$ \uparrow\downarrow\rangle \Rightarrow  \downarrow\downarrow\rangle$ $T_1$ relaxation	Thermalization

TABLE II | Maximum readout visibility for the four spin states of the two-qubit system. The error bar for  $|\uparrow\uparrow\rangle$  state visibility is derived from the fit of ESR driven Rabi oscillations shown in Fig 2d. Similarly, the fit of exchange-driven Rabi oscillations shown in Fig. 1(c) gives the error bar for  $|\downarrow\uparrow\rangle$  state visibility. The exchange driven  $|\downarrow\uparrow\rangle \Leftrightarrow |\uparrow\downarrow\rangle$  oscillation experiment is reported in the Extended Data Fig. 1. The errors for  $|\uparrow\downarrow\rangle$  and  $|\downarrow\downarrow\rangle$  state visibility are derived from the fit of the exponential decay curve between the two states as reported in the Supplementary Information.

$\Delta f_{\text{ESR}}^{\text{QD1}}$  and  $\Delta f_{\text{ESR}}^{\text{QD2}}$ , indicating that any fluctuations are caused by a highly localized effect. We postulate the fluctuations in ESR frequency to be caused by the residual (800 ppm)  $^{29}\text{Si}$  nuclear spins in the isotopically enriched substrate. Similar observations were already published in Ref. 15 on a different device. Figs. 3b-g show the histograms of  $\Delta f_{\text{ESR}}$  at three different magnetic fields for both qubits. We observe that the distribution of  $\Delta f_{\text{ESR}}$  becomes narrower as the magnetic field increases. To better quantify this effect, we plot the standard deviation of  $\Delta f_{\text{ESR}}^{\text{QD1}}$  as a function of magnetic field in Fig. 3h and compare it to numerical models for the hyperfine-interaction during electron singlet initialization, ESR drive, and ST measurement. These models indicate that nuclei are largely driven by the microwave ESR drive in conjunction with the anisotropic hyperfine interaction, while other contributions such as “ionization shock” from electron tunneling are negligible. Details of these conclusions and this model may be found in the supplementary material. Furthermore, these numeric simulations indicate that with 800 ppm  $^{29}\text{Si}$ , the total amount of ESR-driven nuclear spin noise can easily vary by two orders of magnitude depending on the particular placement of the nuclear spins relative to the dot. Figure 3h shows traces for 30 simulated quantum dots each with random  $^{29}\text{Si}$  placement, illustrating this variation. At low magnetic fields, reducing ESR frequency drift due to nuclear fluctuations may require additional isotopic purification.

In summary, we have successfully operated spin qubits in a silicon platform with a readout fidelity higher than 99.3 %. The ST readout scheme enables coherent control of single spins at a magnetic field of 150 mT and a resonance frequency as low as 4.1 GHz. Such lower-frequency qubit operation significantly improves the scalability prospects for future silicon quantum processors. In addition, the ST readout technique has enabled a more detailed study of important effects in magnetic noise, which becomes more profound when silicon qubits are operated in such a low magnetic field environment. Despite using an isotopically enriched  $^{28}\text{Si}$  substrate, there remain residual  $^{29}\text{Si}$  nuclear spins located in the vicinity of the qubits, causing fluctuations in the qubit operation frequencies. We observe

the nuclear spin flip rate to increase as the applied external magnetic field decreases, an effect that can be reduced in future devices by increasing the  $^{28}\text{Si}$  isotopic enrichment.

## METHODS

Figs. 1a and b show a scanning electron micrograph and a cross-sectional schematic of the sample used in this study. It is fabricated on top of a 900 nm thick, isotopically enriched  $^{28}\text{Si}$  epi-layer with 800 ppm residual  $^{29}\text{Si}$  on a natural silicon substrate<sup>30</sup>. We first grow a 7 nm thick thermal  $\text{SiO}_2$  plus a 3 nm atomic layer deposition (ALD) aluminium oxide to prevent gate to substrate leakage. Then, we use electron-beam lithography to write the nanoscale gate pattern and perform resist development in pre-cooled ( $-20^\circ\text{C}$ ) Methyl Isobutyl Ketone solution with ultrasound agitation. In the next step, we evaporate Pd onto the chip to form the gate electrodes. Since Pd has a much smaller grain size than aluminium, we routinely achieve gate features as narrow as 12 nm. A 2 nm thin Titanium (Ti) layer is evaporated prior to Pd deposition to enhance the cohesion of the Pd gate onto the oxide. The above lithography process is repeated several times to form the stack of Pd gate electrodes. Since Pd does not have a native oxide, we use ALD to grow 3-4 nm aluminium oxide on top of the gates to provide electrical insulation between different layers. Lastly, the sample is annealed in forming gas at  $400^\circ\text{C}$  for 15 mins to repair the damage caused by lithography.

Stanford Research Systems SIM928 modular programmable voltage sources are used to dc-bias all gate electrodes shown in Fig. 1a and b. In addition, voltage pulses from an arbitrary waveform generator (Tektronix AWG7122) are applied to G1 and G3 through a voltage combiner. The bandwidth for dc bias (ac pulses) is 30 Hz (80 MHz). We use a nanoscale on-chip integrated 40-GHz antenna to generate the ac magnetic field to drive the electron spin resonance<sup>31</sup>. The antenna is powered by a vector microwave source (Agilent E8267D PSG). The sample is cooled down in an Oxford Instruments, liquid-helium cooled, dilution

refrigerator with magnet. All measurements are performed at the phonon bath temperature of 37 mK.

## ACKNOWLEDGMENTS

We thank W. Huang for enlightening discussions and A. Saraiva for helpful comments on the  $^{29}\text{Si}$  nuclear spin modeling. We acknowledge support from the Australian Research Council (CE170100012), the US Army Research Office (W911NF-17-10198) and the NSW Node of the Australian National Fabrication Facility. The views and conclusions contained in this document are those of the authors and should not be interpreted as representing the official policies, either expressed or im-

plied, of the Army Research Office or the U.S. Government. The U.S. Government is authorized to reproduce and distribute reprints for Government purposes notwithstanding any copyright notation herein. B.H. acknowledges support from the Netherlands Organization for Scientific Research (NWO) through a Rubicon Grant. K.M.I. acknowledges support from a Grant-in-Aid for Scientific Research by MEXT, NanoQuine, FIRST, and the JSPS Core-to-Core Program.

## AUTHOR INFORMATION

The authors declare no competing financial interests. Readers are welcome to comment on the online version of the paper. Correspondence and request for materials should be addressed to R.Z. (ruichen77@gmail.com) or A.S.D. (a.dzurak@unsw.edu.au).

\* Present address: National Institute of Standards and Technology, 325 Broadway, Boulder, CO 80305, United States.

† Present address: Microsoft Quantum, The University of Sydney, Sydney, NSW 2006, Australia.

‡ Present address: Research and Prototype Foundry, The University of Sydney, Sydney, NSW 2006, Australia.

<sup>1</sup> A. M. Tyryshkin *et al.*, *Nature materials* **11**, 143 (2012).

<sup>2</sup> J. T. Muhonen *et al.*, *Nature Nanotechnology* **9**, 986 (2014).

<sup>3</sup> M. Veldhorst *et al.*, *Nature Nanotechnology* **9**, 981 (2014).

<sup>4</sup> T. D. Ladd and M. S. C., *Encyclopedia of Modern Optics (Second Edition)*, 467 (2018).

<sup>5</sup> R. Maurand *et al.*, *Nature Communications* **7**, 13575 (2016).

<sup>6</sup> M. Veldhorst, H. G. J. Eenink, C. H. Yang, and A. S. Dzurak, *Nature communications* **8**, 1766 (2017).

<sup>7</sup> L. Hutin *et al.*, in *2018 48th European Solid-State Device Research Conference (ESSDERC)* (2018) pp. 12–17.

<sup>8</sup> L. Vandersypen, H. Bluhm, J. Clarke, A. Dzurak, R. Ishihara, A. Morello, D. Reilly, L. Schreiber, and M. Veldhorst, *npj Quantum Information* **3**, 34 (2017).

<sup>9</sup> J. M. Elzerman *et al.*, *nature* **430**, 431 (2004).

<sup>10</sup> E. Kawakami, P. Scarlino, D. R. Ward, F. Braakman, D. Savage, M. Lagally, M. Friesen, S. N. Coppersmith, M. A. Eriksson, and L. Vandersypen, *Nature nanotechnology* **9**, 666 (2014).

<sup>11</sup> K. Takeda, J. Kamioka, T. Otsuka, J. Yoneda, T. Nakajima, M. R. Delbecq, S. Amaha, G. Allison, T. Kodera, S. Oda, *et al.*, *Science advances* **2**, e1600694 (2016).

<sup>12</sup> T. Watson, S. Philips, E. Kawakami, D. Ward, P. Scarlino, M. Veldhorst, D. Savage, M. Lagally, M. Friesen, S. Coppersmith, *et al.*, *Nature* **555**, 633 (2018).

<sup>13</sup> D. M. Zajac *et al.*, *Science* **359**, 439 (2018).

<sup>14</sup> J. Yoneda *et al.*, *Nature nanotechnology* **13**, 102 (2018).

<sup>15</sup> W. Huang *et al.*, arXiv preprint arXiv:1805.05027 (2018).

<sup>16</sup> C. H. Yang *et al.*, arXiv preprint arXiv:1807.09500 (2018).

<sup>17</sup> X. Xue, T. Watson, J. Helsen, D. Ward, D. Savage, M. Lagally, S. Coppersmith, M. Eriksson, S. Wehner, and L. Vandersypen, arXiv preprint arXiv:1811.04002 (2018).

<sup>18</sup> C. Jones *et al.*, *Physical Review X* **8**, 021058 (2018).

<sup>19</sup> T. A. Baart, M. Shafiei, T. Fujita, C. Reichl, W. Wegscheider, and L. M. K. Vandersypen, *Nature nanotechnology* **11**, 330 (2016).

<sup>20</sup> T. Fujita, T. A. Baart, C. Reichl, W. Wegscheider, and L. M. K. Vandersypen, *npj Quantum Information* **3**, 22 (2017).

<sup>21</sup> M. A. Fogarty *et al.*, *Nature communications* **9**, 4370 (2018).

<sup>22</sup> A. C. Johnson, J. R. Petta, C. M. Marcus, M. P. Hanson, and A. C. Gossard, *Phys. Rev. B* **72**, 165308 (2005).

<sup>23</sup> W. A. *et al.*, *Nature Nanotechnology*, 1 (2019).

<sup>24</sup> P. Pakkiam, A. V. Timofeev, M. G. House, M. R. Hogg, T. Kobayashi, M. Koch, S. Rogge, and M. Y. Simmons, *Phys. Rev. X* **8**, 041032 (2018).

<sup>25</sup> M. Urdampilleta *et al.*, arXiv preprint arXiv:1809.04584 (2018).

<sup>26</sup> M. Pioro-Ladriere, T. Obata, Y. Tokura, Y.-S. Shin, T. Kubo, K. Yoshida, T. Taniyama, and S. Tarucha, *Nature Physics* **4**, 776 (2008).

<sup>27</sup> T. Ito *et al.*, arXiv preprint arXiv:1805.06111 (2018).

<sup>28</sup> A. Crippa, R. Ezzouch, A. Aprá, A. Amisse, L. Houtin, B. Bertrand, M. Vinet, M. Urdampilleta, T. Meunier, M. Sanquer, *et al.*, arXiv preprint arXiv:1811.04414 (2018).

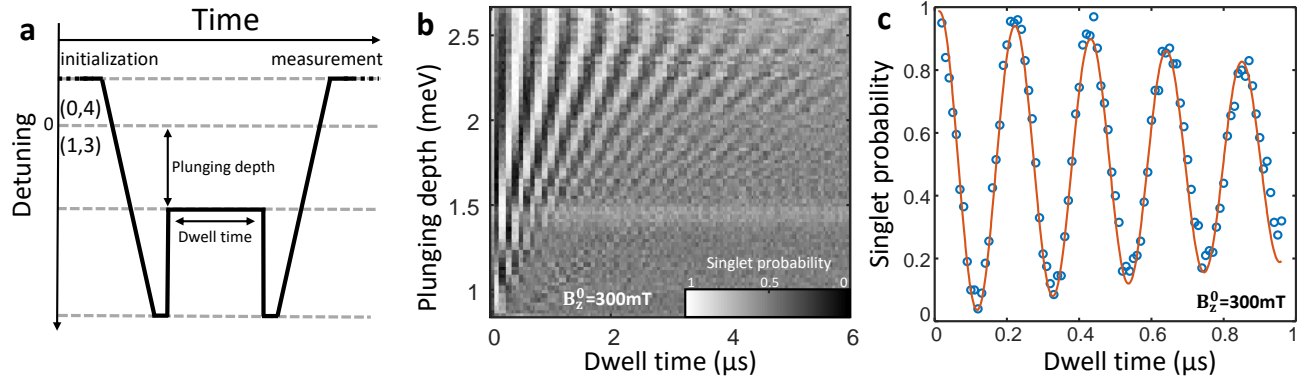
<sup>29</sup> M. Brauns, S. V. Amitonov, P. Spruijtenburg, and F. A. Zwanenburg, *Scientific reports* **8**, 5690 (2018).

<sup>30</sup> K. M. Itoh and H. Watanabe, *MRS Communications* **4**, 143157 (2014).

<sup>31</sup> J. P. Dehollain, J. J. Pla, E. Siew, K. Y. Tan, A. S. Dzurak, and A. Morello, *Nanotechnology* **24**, 015202 (2012).

<sup>32</sup> C. H. Yang, W. H. Lim, F. A. Zwanenburg, and A. S. Dzurak, *AIP Advances* **1**, 042111 (2011).

<sup>33</sup> P. Harvey-Collard *et al.*, *Physical Review X* **8**, 021046 (2018).



**Extended Data Figure 1 | Exchange driven oscillations.** **a** Schematic diagram of the pulse sequence to measure the exchange oscillations. First, we initialize the double quantum dots (DQDs) in the  $|\uparrow\downarrow\rangle$  state as described in Fig. 2a. Second, we enable the exchange coupling between the two dots by pulsing to the shallow detuning region. This will drive the coherent oscillations between the  $|\uparrow\downarrow\rangle$  and  $|\downarrow\uparrow\rangle$  states. We then stop the exchange driven oscillations by pulsing back to the deep detuning region. Finally, another adiabatic pulse brings the DQDs from (1,3) back to (0,4) and completes the spin measurement, during which the  $|\uparrow\downarrow\rangle$  state is converted to singlet and the  $|\downarrow\uparrow\rangle$  state is converted to triplet. **b** Singlet probability plotted as a function of plunging depth and dwell time at the shallow detuning region. **c** A single trace of exchange driven oscillation with plunging depths of 1.9 meV. The red solid line indicates is a fit to the Rabi's formula with maximum visibility of  $99.3\pm 2.3\%$ .

- <sup>34</sup> C. R. Rao and M. Statistiker, *Linear statistical inference and its applications*, Vol. 2 (Wiley New York, 1973).  
<sup>35</sup> T. Nakajima *et al.*, Physical review letters **119**, 017701 (2017).  
<sup>36</sup> T. Thorbeck and N. M. Zimmerman, AIP Advances **5**, 087107 (2015).  
<sup>37</sup> L. V. C. Assali, H. M. Petrilli, R. B. Capaz, B. Koiller, X. Hu, and S. D. Sarma, Phys. Rev. B **83**, 165301 (2011).  
<sup>38</sup> D. K. Wilson, Phys. Rev. **134**, A265 (1964).  
<sup>39</sup> A. L. Saraiva, M. J. Calderón, R. B. Capaz, X. Hu, S. D. Sarma, and B. Koiller, Phys. Rev. B **84**, 155320 (2011).  
<sup>40</sup> J. L. Ivey and R. L. Mieher, *Phys. Rev. B* **11**, 849 (1975).  
<sup>41</sup> A. Abragam, *Principles of Nuclear Magnetism* (Oxford, 1961) Chap. IX.III.B.  
<sup>42</sup> K.-M. C. Fu, T. D. Ladd, C. Santory, and Y. Yamamoto, Phys. Rev. B **69**, 125306 (2004).  
<sup>43</sup> J. J. Pla, F. A. Mohiyaddin, K. Y. Tan, J. P. Dehollain, R. Rahman, G. Klimeck, D. N. Jamieson, A. S. Dzurak, and A. Morello, *Phys. Rev. Lett.* **113**, 246801 (2014).

## SUPPLEMENTAL INFORMATION

### $T_1$ relaxation measurement

In this study, we use  $T_1$  relaxation from the  $|\uparrow\downarrow\rangle$  to the  $|\downarrow\downarrow\rangle$  state as an alternative method to assess maximum readout visibilities. We first initialize the double-quantum-dot (DQD) system in  $|\uparrow\downarrow\rangle$  as described in Fig. 2a. The DQD system then dwells in the (1,3) region for the  $|\uparrow\downarrow\rangle$  state to decay to the  $|\downarrow\downarrow\rangle$  state. Finally, we pulse the DQD back to the (0,4) region for spin readout. The  $|\uparrow\downarrow\rangle$  state is converted to singlet while the  $|\downarrow\downarrow\rangle$  state is converted to triplet. As shown in Fig. S1, the singlet probability decays exponentially with dwell time. To more accurately determine the maximum readout visibility of the  $|\uparrow\downarrow\rangle$  state, we perform eight  $T_1$  relaxation measurements with  $0.1\ \mu\text{s}$  dwell time. Each of the measurements consists of 200 single-shot readout events. We expect  $|\uparrow\downarrow\rangle$  to maintain its spin state as this dwell time is orders of magnitude shorter than the  $T_1$  time. We observe the mean of the singlet probability of these eight measurements to be  $99.5\pm 0.7\%$ . This is the maximum experimentally observed visibility for the  $|\uparrow\downarrow\rangle$  state and is consistent with the readout fidelity reported in the main text. Similarly, we extract the maximum readout visibility for the  $|\downarrow\downarrow\rangle$  state to be  $96.8\pm 1.0\%$  by setting the dwell time to 0.7 sec. This value could be limited by the 120 mK electron temperature of our system. We estimate the probability of the  $|\downarrow\downarrow\rangle$  state to be thermally excited to the  $|\uparrow\downarrow\rangle$  state to be  $P_{\text{excited}} = 1 - \exp(-g\mu_B B_z^0/k_B T_{\text{electron}}) = 3.4\%$ , where  $g \approx 2$  is the gyromagnetic ratio of the electron,  $\mu_B$  is the Bohr magneton,  $k_B$  is the Boltzmann constant and  $T_{\text{electron}}$  is the electron temperature of the device.

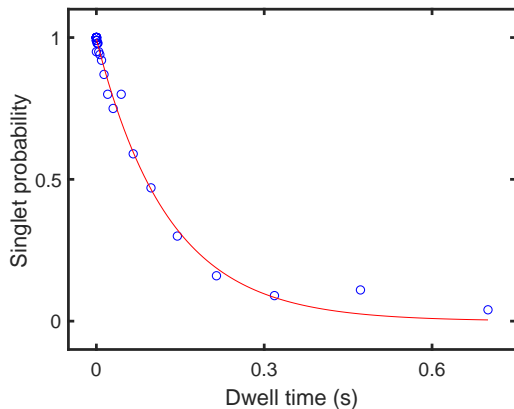


**Figure S1 |  $T_1$  relaxation measurement.** Decay of the  $|\uparrow\downarrow\rangle$  state to the  $|\downarrow\downarrow\rangle$  state as a function of dwell time. The red line is a fit to an exponential decay, indicating a relaxation time of  $129 \pm 9$  ms. Each data point is derived from 200 single-shot singlet-triplet readout events. All measurements are performed in an external dc magnetic field of 300 mT.

### Electrostatic and Hyperfine Modeling

In this section, we seek a model which is consistent with basic dot characterizations as well as the observed field-dependent ESR frequency shifts. We attribute the detected drift of the ESR frequencies for these quantum dots to fluctuating nuclear magnetization. Thus, we seek to identify and quantitatively model the nature of the magnetic-field dependent process driving nuclear spin flips. As we will argue, the nuclei flip due to the ESR drive in conjunction with the anisotropic hyperfine interaction. To support this conclusion, we first quantify the strength of hyperfine interactions inside each quantum dot, and then build a statistical model for the local magnetic fields. We find that the amount of variation of the ESR frequency in the quantum dots is highly consistent with our model.

#### 1. Electrostatic wavefunction model

The shape and size of the electron wavefunction defines the degree of overlap with nearby residual  $^{29}\text{Si}$  nuclear spins. We start with a calculation of the anticipated wavefunction envelope. To quantify the electron confinement in the inner (quantum) area under the G1 and G3 gates, we have performed self-consistent Schrödinger-Poisson simulations of the device. For this, we construct a virtual three dimensional multilayer and multimaterial device geometry from the production masks and models of the fabrication steps. An image of the virtual 3D stack appears in Fig. S2a.

Internal stress is expected to build up when cooling this heterogeneous system to cryogenic temperatures. We have solved the stationary stress-strain problem for the entire layout to incorporate the resulting strain

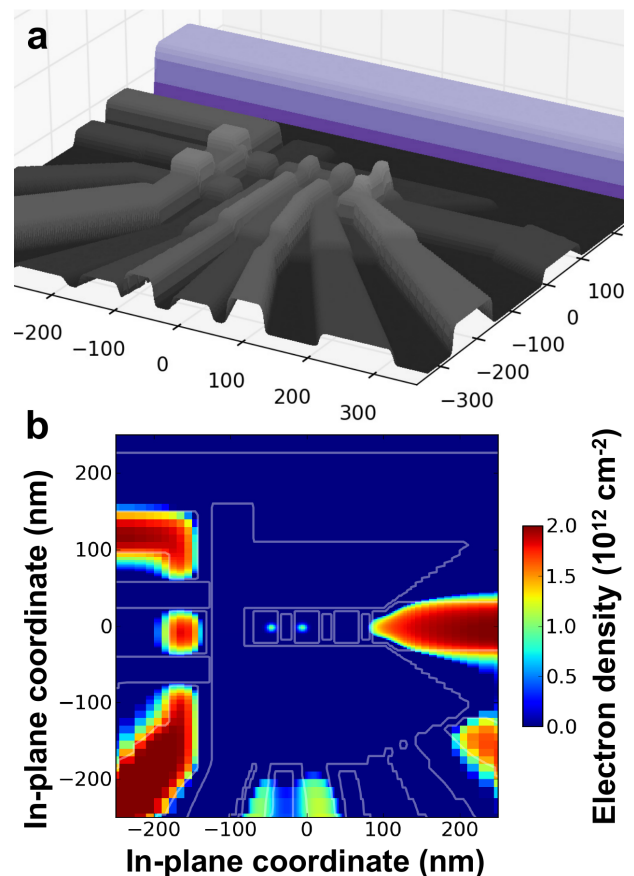


**Figure S2 | Self-consistent Schrödinger-Poisson simulations of the device.** **a**, A projection of the full device model layout, showing its ALD-clad top surface (gray) with the ESR line (purple) in the back. **b**, Simulated charge accumulation along the Si/SiO<sub>2</sub> interface in a nominally tuned device, with the partitioned 2DEG of the sensing SET circuit visible in the left, reservoir puddle in the right, and a pair of interacting electrons in the center, confined by the electrostatically-defined double quantum dot potential.

pattern into the electron potential profile as a correction<sup>36</sup>. In principle, voids or cracks could form somewhere in the physical device, thus dramatically changing the stress-strain problem, but our simulation treats all constituent layers as perfectly bonded ideal materials. Another issue is that the reliability and consistency of literature values for elastic parameters of many of the materials in the gate stack is low, and, beyond that, their applicability down to the scale of tens of (and even few) nanometers is questionable. However, we find that for this device the strain-induced correction to the potential profile for electrons accumulated at the Si/SiO<sub>2</sub> interface is up to a few meV at most, so the limited precision of this calculation is of only modest consequences given the magnitude of voltage biasing applied to the device.

We employ the Thomas-Fermi approximation to model the partitioned 2-dimensional electron gas

(2DEG), and full quantum-mechanical treatment of one- and two-electron quantum dot states in the inner area. Figure S2b gives one example of a simulated charge accumulation. When the gates are tuned close to the biases used in the experiments (in which the exchange  $J$  between two separated electrons is relatively low), we calculate single-electron quantization energies of  $\hbar\omega \sim 16$  meV perpendicular to the potential trough and up to  $\sim 11$  meV along it. These quantization energies define the spatial extent of the electron eigenstate. Using  $m \approx 0.2m_0$  for the relevant electron effective mass in Si along oxide interface, the extent  $d$  (defined here by the contour of  $1/e$  reduction of the electron charge density from its maximal value in the center of the quantum dot) is, approximately,  $40 \text{ nm}/\sqrt{\hbar\omega}$  [in meV], i.e., the electron state is about  $10 \times 12 \text{ nm}^2$  for the quoted quantization energies. The electron is pressed towards the Si/SiO<sub>2</sub> interface by the mean electric field  $F \sim 20$  mV/nm. These values should be treated cautiously, since our multi-gate MOS device allows substantial flexibility in tuning. Also, in this effort, we have chosen to forego any possible contribution of potential disorder associated with the silicon-oxide interface and/or discrete charges trapped in the oxide.

## 2. Hyperfine interactions

The wavefunction sizes derived in the previous section feed into well-known interaction physics between the electron spins in the quantum dot and the <sup>29</sup>Si nuclei<sup>37</sup>. For these, we simplify our model drastically by treating 2 or 4 electrons in the dot as empty relative to hyperfine interactions, since overlapping electrons paired into singlet states have no net hyperfine interaction. Likewise, we treat 3 electrons as a single electron relative to spin interactions, neglecting the closed shell. We acknowledge that the charge distribution of three electrons certainly exceeds that of a single electron, but note that our ability to determine the wavefunction size can only be approximate and hence we omit the complexities of this detail.

For a single, singly or triply occupied quantum dot and for nuclei close to the electrons, the largest hyperfine interaction is the Fermi-contact interaction, with hamiltonian

$$H_{\text{en-contact}} = \hbar \sum_j A_j \mathbf{S} \cdot \mathbf{I}_j, \quad (\text{S1})$$

where  $\mathbf{S}$  is the single electron vector spin operator,  $\mathbf{I}_j$  is the vector spin operator for the  $j$ th <sup>29</sup>Si nucleus, and the contact coefficient  $A_j$  in units of rad/sec is

$$A_j = \frac{2}{3} \mu_0 g \mu_B \gamma \eta \frac{8}{a^3} |\psi(\mathbf{r}_j)|^2 \cos^2(k_0 x_j + \phi). \quad (\text{S2})$$

Here  $\gamma/2\pi = -8.467$  MHz/T is the gyromagnetic ratio for a <sup>29</sup>Si nucleus,  $\eta = 178$ <sup>38</sup> is the Bloch wavefunction overlap, and  $a = 0.543$  nm is the lattice constant

of silicon. The  $\cos^2(k_0 x_j + \phi)$  term arises due to the mixing of 2 equivalent valley states along the growth axis, for which  $k_0$  is the wavenumber at the conduction-band minimum and  $\phi$  a field-dependent phase offset, and the smooth envelope wavefunction  $\psi$  is normalized such that, when summing over *all* lattice sites  $r_k$ ,  $\sum_k |\psi(\mathbf{r}_k)|^2 \cos^2(k x_k + \phi) = 1$ . Note that here we put the wafer-normal direction as  $x$  and the direction of the in-plane magnetic field as  $z$  to conform to common conventions in electron-nuclear magnetic resonance.

Since the contact hyperfine term provides the largest shift of the effective magnetic field as seen by the electron, we estimate the total Overhauser shift as simply

$$\delta\omega = \sum_j A_j \langle I_j^z \rangle, \quad (\text{S3})$$

for some configuration of nuclear spin projections  $\langle I_j^z \rangle$ .

The contact hyperfine term is not the only term present; we observe the effects of the electron-nuclear dipole-dipole interaction, with hamiltonian

$$H_{\text{en-dipole}} = \hbar \frac{\mu_0}{4\pi} g \mu_B \gamma \sum_j \int d\mathbf{r} |\Psi(\mathbf{r})|^2 \times \frac{3[(\mathbf{r} - \mathbf{r}_j) \cdot \mathbf{S}][(\mathbf{r} - \mathbf{r}_j) \cdot \mathbf{I}_j] - |\mathbf{r} - \mathbf{r}_j|^2 \mathbf{S} \cdot \mathbf{I}_j}{|\mathbf{r} - \mathbf{r}_j|^5}, \quad (\text{S4})$$

where the sum over  $j$  is the sum over <sup>29</sup>Si nuclei and  $\Psi(\mathbf{r})$  is the total wavefunction of the electron in the dot. We approximate the dipole-dipole interaction by breaking this integral into two terms. The first term, which we refer to as the central-cell dipole-dipole interaction, ignores envelope variation and focuses on the microscopic integral over the vicinity of the <sup>29</sup>Si in question. For all other cells, we consider a second macroscopic term in which we neglect variation in  $\Psi(\mathbf{r})$  over individual cells and rather replace the integral with a sum including the sampled  $(|\psi(\mathbf{r}_k)|^2 - |\psi(\mathbf{r}_j)|^2) \cos^2(k x_k + \phi)$ . The  $\psi(\mathbf{r}_j)$ -part can be done explicitly and is an adjustment to the central-cell term. Both terms combine to a tensor coupling of the electron spin to the nuclear spin of the form  $\mathbf{S} \cdot \mathbf{D} \cdot \mathbf{I}_j$ , and the traceless tensor  $\mathbf{D}$  possesses both diagonal and off-diagonal terms. The diagonal terms behave similarly to the contact hyperfine interaction, in that a nuclear flip due to this term is always accompanied by an electron flip, therefore costing the electron Zeeman energy  $g \mu_B B_z^0$ . However, these dipole-dipole diagonal terms are nearly two orders of magnitude smaller than the contact terms, as calculated in Ref.<sup>37</sup>, and so may be neglected.

Much more critical for our model of hyperfine dynamics are off-diagonal terms of the coupling tensor  $\mathbf{D}$ , as these may allow nuclear spin flips without associated electron flips, effectively forming a correction in the local field direction of the nucleus due to the electron spin's polarization. We find that the symmetry of the wavefunction in the valley-mixed state leaves one of the off-diagonal components of the central-cell dipole-dipole coupling tensor non-zero, namely the in-plane

$D_j^{zy}$  term. We evaluate this central-cell off-diagonal term using the plane-wave expansion of the periodic Bloch amplitude, with the numerical coefficients reported in Ref. 39. Handily, integrals are dominated by the volume away from the nucleus, where the expansion is more accurate. With  $y, z$  along main crystal axes, we find a total estimate of  $D_j^{zy}$  as

$$D_j^{zy} \approx \frac{\mu_0}{4\pi} g\mu_B\gamma \left[ 0.6|\psi(\mathbf{r}_j)|^2 \sin(2k_0x_j+2\phi) \left( \frac{4}{\sqrt{3}a} \right)^3 + \sum_{k \neq j} |\psi(\mathbf{r}_k)|^2 \cos^2(k_0x_k + \phi) \frac{3z_{kj}y_{kj}}{r_{kj}^5} \right], \quad (\text{S5})$$

where  $\mathbf{r}_{kj} \equiv (x_{kj}, y_{kj}, z_{kj}) = \mathbf{r}_k - \mathbf{r}_j$ . The central cell part diminishes for other field directions (and vanishes for fields along [110] equivalents). This expression is notably dependent on the valley mixing phase at the nucleus. We caution that this expression is approximate, as microscopic integrals over neighboring cells interfere with the terms we have included. For the estimate above, the ratio of the central-cell anisotropic off-diagonal term to the contact hyperfine term for a typical nucleus  $j$  is a factor of about  $10^{-3}$ , which is similar to the experimentally confirmed ratio of the same for many  $^{29}\text{Si}$  nuclear sites of a  $^{31}\text{P}$  donor<sup>40</sup>, with pronounced exceptions from some of the nuclei very close to the donor.

### 3. Model of nuclear dynamics

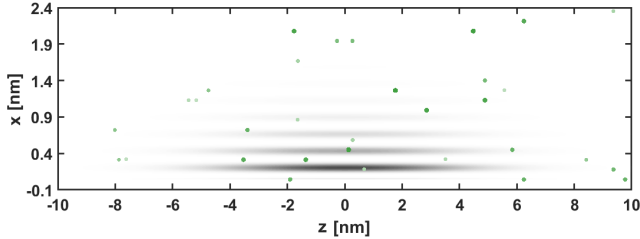


**Figure S3 |Example nuclear configuration.** The grey shaded area is an indication of the model for the envelope square wavefunction  $|\psi(\mathbf{r})|^2 \cos^2(k_0x + \phi)$ . The green dots indicate possible locations of  $^{29}\text{Si}$  nuclei, chosen by randomly placing  $^{29}\text{Si}$  at lattice sites with a probability of 800 ppm. The dot size depicts the proximity of each nucleus to the viewer in this projection; the box size is  $20 \times 20 \times 2.5 \text{ nm}^3$  in this picture, although a bigger box of size  $50 \times 50 \times 5 \text{ nm}^3$  is used in calculations.

For numeric simplicity in forming a statistical model of nuclear dynamics, we employ a simplified model for the quantum dot wavefunction shape informed by the electrostatic calculations above. We consider a simple transverse wavefunction with a Gaussian shape and a  $1/e$  diameter of  $|\psi(\mathbf{r})|^2$  of 11 nm. In the vertical direction, we consider an Airy function corresponding to

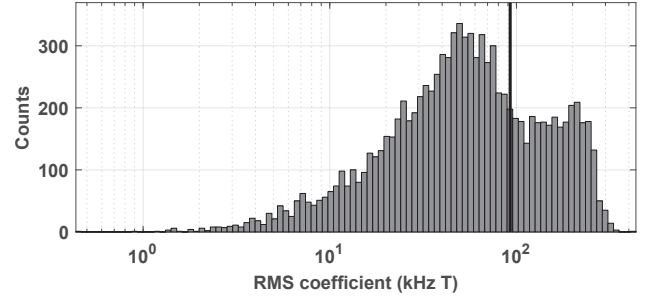


**Figure S4 |Distribution of RMS deviation coefficients.** The histogram counts instances for when the fit coefficient  $c$ , for which the RMS deviation of the ESR frequency varies as  $c/B_z^0$ , falls within the indicated bin, for a total population of 10,000 random  $^{29}\text{Si}$  placements. The vertical black line indicates the location in this distribution corresponding to the fit of the experimentally observed data, indicating a typical population member.

vertical electric field 20 mV/nm. This wavefunction is shown relative to the density of  $^{29}\text{Si}$  for 800 ppm content in a sample nuclear configuration depicted in Fig. S3. For this random configuration, 10 nuclei have  $A_j/2\pi > 100 \text{ kHz}$ . Another random configuration may have more, or less. As we will see, the impact of various hyperfine terms varies considerably depending on where the  $^{29}\text{Si}$  nuclei happened to have landed relative to the small dot and its valley oscillations.

We have found that the dominant term driving nuclear spin flips in the experiments of this manuscript is from the combination of a tilted local magnetic field for each nucleus due to the anisotropic dipole-dipole interaction in conjunction with the driving of ESR frequencies at the sum or difference frequencies of the electron and nuclear Zeeman frequencies. This interaction, when driven for times long relative to thermal relaxation times, has been understood for many decades to lead to dynamic nuclear polarization in silicon donor ensembles<sup>41</sup>. In these experiments the process is referred to as the “solid-state effect.” To summarize the interaction, consider a single nucleus and a single electron. In the rotating-wave-approximated frame rotating at the applied ESR frequency  $\omega$ , and keeping only the secular terms of the hyperfine interaction, the hamiltonian term for nucleus  $j$  is

$$H_j = (\omega - g\mu_B B_z^0/\hbar) S^z + \gamma B_z^0 I_j^z + A_j S^z I_j^z + \Omega S^x + D_j^{zy} S^z I_j^y, \quad (\text{S6})$$

where  $B_z^0$  is the applied magnetic in-plane field in the  $z$  direction. Because the anisotropic dipolar interaction coefficient  $D_j^{zy}$  is by far the smallest term in this expression, it may be treated as a perturbation. In the interaction picture, we find that due to the Rabi drive at rate  $\Omega$ , the interaction-picture perturbation has oscillatory terms at frequencies  $\omega - g\mu_B B_z^0/\hbar \pm \gamma B_z^0$ . When

integrating to first order in  $D_j^{zy}/|H|$  for a Rabi drive of duration  $\tau$ , at the peak frequencies  $\omega = (g\mu_B/\hbar \pm \gamma)B_z^0$ , the first-order probability of a nuclear spin flip is  $p_j = (1/32)(\Omega\tau)^2(D_j^{zy}/\gamma B_z^0)^2$ . For the experiment with results shown in Fig. 3 in the main text, the pulse duration was  $\tau = 100 \mu\text{s}$ , and the Rabi drive may be estimated as approximately  $\pi/(1 \mu\text{s})$ , although the Rabi drive was not calibrated in this experiment the same as would be indicated by Fig. 2e of the main text. Under these conditions, the peak probability of a flip per Rabi pulse scales as  $(1/B_z^0)^2$ , varies substantially from one  $^{29}\text{Si}$  to the next, and may be as high as  $10^{-4}$  for well coupled nuclei at low magnetic field. When a flip does happen, the Overhauser shift  $\delta\omega$  changes by  $A_j$ ; hence the variance of such shifts for a single nucleus in  $N$  events is approximately  $NA_j^2 p_j(1-p_j)$ . We estimate the total variance of observed frequency shifts by summing the variance of all nuclei (treated, appropriately, as independent), for a number of trials given by the number of single shot measurements used at each applied frequency (200) times the number of frequency sweeps in the data (70). We approximate in this calculation that each sweep over the ESR frequency always hits each resonance once.

The ESR drive is not the only process that causes a change in a nucleus' local transverse field, enabling a spin flip. We have also considered the probability that the process of the electron tunneling suddenly changing the local magnetic field of a nuclear spin ("ionization shock"), may cause a nuclear flip. The associated probability of a flip may be estimated as the squared amplitude of the first-order perturbative mixing of two nuclear spin states due to a particular hyperfine term<sup>42,43</sup>. For the contact hyperfine term, this probability is approximately  $(1/16)[\hbar A_j/(g\mu_B B_z^0)]^2$ . For the anisotropic dipolar term, this probability is approximately  $(1/16)[D^{zy}/(\gamma B_z^0 \pm A_j)]^2$ . These probabilities are lower than the ESR-induced flip probabilities discussed above, but they may occur for every single measurement for every frequency swept in the experiment.

Other mechanisms for flipping nuclei are even smaller. We also consider the probabilities of nuclear-nuclear flip-flop due to the contact hyperfine term when the dot is occupied by an electron. We consider the coherent evolution of each nuclear pair in their local hyperfine field due to this effective interaction, and calculate the variance of ESR frequency shifts assuming each nuclear pair is independent.

Notably, all of the nuclear flip probabilities above scale as the inverse square of the applied field,  $(1/B_z^0)^2$ . As the probabilities are very small, calculated variances may be simply summed and each are proportional to the associated probability and therefore to  $(1/B_z^0)^2$ ; the

root-mean-square (RMS) deviation therefore scales as  $1/B_z^0$ , as seen in the experimental data. The question to be answered by our modeling above is whether the amplitude of that variation numerically matches the data. We find that our model is consistent with the

TABLE S1 | Simulated contributions to ESR variance

Nuclear-flip process	Contribution
ESR drive on anisotropically mixed states	99.2%
ionization shock from anisotropic dipolar hyperfine-mediated interactions	0.4%
ionization shock from contact terms	0.3%

data; Fig. 3h of the main text shows example RMS frequency deviations as calculated by finding all probabilities and variances for all  $^{29}\text{Si}$  nuclei as a function of magnetic field for 30 virtual sample crystals. We find that some simulated samples have a higher standard deviation than the data, and some lower.

To evaluate the typicality of our real sample, we look at the coefficient for the RMS frequency derivation,  $c$ , such that  $\Delta f_{\text{ESR}} = c/B_z^0$ . We calculate  $c$  for 10,000 virtual samples in which the 800 ppm  $^{29}\text{Si}$  are randomly placed relative to the wavefunction. The resulting distribution of coefficients is extremely broad and the experimentally observed data sits near the mean of the distribution. We further find that in our simulation the variance is highly dominated by the ESR-driving term relative to other spin-flip processes we considered. Averaged over those virtual samples with a coefficient  $c$  within a factor of 2 of the experimentally observed coefficient, we find that 99.4% of the variance results from the "solid-state effect," i.e. ESR driving on states mixed by the off-diagonal anisotropic dipolar interaction. The much smaller contribution of the other interactions we considered is shown in Table S1.

Although other processes are certainly at play which may influence the drift of the ESR frequency, we find the theory we have presented here to be highly consistent with the observed data, using a model with only physically constrained parameters. While many approximations were necessary to estimate the wavefunction size and the nuclear spin-flip probabilities, the broad distribution of outcomes provided by the random placement of 800 ppm  $^{29}\text{Si}$  in the small wavefunction means that small deviations from these approximations would not be discernible. Our model also indicates that the dominant source of the variance would be reduced substantially if using an out-of-plane magnetic field, since the off-diagonal anisotropic dipolar interaction which provides the bulk of the spin-flip variance in our model would be substantially smaller in this orientation.